TECHNISCHE MECHANIK
an open access journal

journal homepage: www.ovgu.de/techmech

Tech. Mech., Vol. 44, Is. 2, (2024), 82–99

Received: 18.07.2024
Accepted: 29.07.2024
Available online: 29.07.2024

Investigation of three-body abrasive wear systems with hard particles and liquid as intermediate medium using a customized tribometer

R. Bilz[1]*, A. I. Ochoa Diaz[1] and K. M. de Payrebrune[1]

[1] RPTU Kaiserslautern-Landau, Institute for Computational Physics in Engineering, Gottlieb-Daimler-Straße 44, 67663 Kaiserslautern, Germany

Abstract: This article discusses dynamic phenomena and the measurement of forces in short-term tests of tribological three-body abrasive wear systems with hard silicon carbide particles. Tribometers enable the measurement of forces, whereby analytical methods are used to determine the forces transmitted in the tribological contact zone on the basis of the forces recorded with a dynamometer that is not directly located in the tribological contact zone. In addition to the theoretical background, this article also deals with a realization of the tribometer, which requires some finely tuned adaptations compared to the ideal tribometer due to tolerances existing in reality. The data basis for the evaluation is a series of experiments with three-body abrasive wear systems with and without liquid, different particle sizes, particle quantities, loads and speeds. In contrast to many other publications, the focus is not only on mean values, but also on the relative spread (i. e. the standard deviation per mean value) of occurring forces. In particular, the relative spread shows clear and repeatable trends and thus qualifies as a supporting criterion for the comparison of different force measurements of tribological systems. Furthermore, an alternative to the established procedure of randomized test execution is presented in order to detect (unintentional) temporal changes in the test conditions.

Keywords: tribometer tests, three-body wear system, dynamics, hard particles, liquid

1 Introduction

The variety of possible effects in tribological systems results in the fact that the prediction capability of models is generally limited and there is no alternative to tribological experiments. The economic importance of tribological contacts is evident from their high share of around 23 % of global energy consumption, ref. Holmberg and Erdemir (2017). According to Czichos and Habig (2020), the most significant wear mechanism for the entire economy is abrasion. In particular, tribological systems in which loose particles are present between the two first bodies have not yet been sufficiently researched (Stachowiak (2014)).

The proportions of different wear mechanisms can usually only be determined experimentally (Czichos and Habig (2020)). Tribological systems can be realized and investigated with the help of test stands. Among others, test stands enable the investigation of wear phenomena, wear rates or coefficients of friction. In Chang et al. (2000) wear mechanisms during lapping are investigated. Li et al. (2022) investigates the coefficient of friction as a function of the sliding speed for different particle sizes on the one hand and wear rates and forms of wear on the other. In Prost et al. (2021), periodic patterns in the measurement data are uncovered using frequency analyses. The large number of studies relate to a wide variety of systems and also focus on very different aspects. Depending on the objective of the study, the influences of the sliding speed (Vashishtha and Sapate (2017)), particle size (Sahariah et al. (2018)) or even both (Yousif et al. (2010)) are taken into account, to name just a few examples. Different subsets of the abundance of parameters are relevant in the studies, and of course this determines which measured values must be recorded and how they are processed and evaluated.

However, wear and friction are quantities that are dependent on both the material pairing and the system, ref. Blau (2001). The comparability of different tribological systems and the transferability of findings from one investigation to other situations is therefore only possible to a very limited extent.

One way of evaluating the comparability of different data sets without knowing all the parameters could be an extended analysis of the data collected as a result of a tribological experiment that has already been carried out. Using recorded time series of forces, not only mean values and coefficients of friction can be determined, but also many other statistically established measures, including, for example, the standard deviation for evaluating the scatter. In addition to the coefficient of friction, the relative spread (i. e. here the standard deviation per mean value) could be precisely one of these measures. In this study, tribological experiments are shown which, on the one hand, exhibit excellent repeatability and, on the other hand, show significant effects of this relative spread due to parameter variations. The evaluation of the spread, even in its simplest form, could therefore be an indicator of differences between various experiments, and possibly also indicate or reveal unintended discrepancies between two experiments.

Sect. 2 first presents an ideal test stand, followed by the realization, including the existing differences, and outlines a test series to demonstrate the influences of various parameters in three-body abrasive wear systems. Sect. 3 deals with the results and discussion of this test series. Sect. 4 summarizes the main features of the publication.

* E-mail address: raphael.bilz@rptu.de
doi: 10.24352/UB.OVGU-2024-057

2 Material and methods

This section deals with the experimental setup and the materials used. In Sect. 2.1, an idealized test stand is considered in the form of a simple analytical model. The realization of the test stand is then presented in Sect. 2.2 and the test series is presented in Sect. 2.3.

2.1 Ideal test stand

Forces occurring in tribological systems are often measured, for example to determine the coefficient of friction. Forces can be measured with dynamometers. However, the dynamometer measures forces that, depending on the installation position and orientation, must first be converted in order to determine the forces that occur directly between the base and counter body. An example of a measurement setup is sketched in Fig. 1 (left).

2.1.1 Determination of the forces in the tribological contact zone

In this system, the lower first body (counter body) moves horizontally, while the upper first body (base body), consisting of the sample, dynamometer and weight, can only move vertically. The dynamometer consists of elements rigidly tied to the weight and an element rigidly tied to the sample. The forces transmitted between these two element groups are translated into electrical signals by force sensors and further processed with the aid of the measuring electronics. Assuming that all bodies under consideration are rigid, especially the force sensors, the forces $\vec{F} = \begin{bmatrix} F_\mathrm{x} & F_\mathrm{y} & F_\mathrm{z} \end{bmatrix}^T$ can be determined between the base body and counter body using the forces recorded in the dynamometer $\vec{F}_\mathrm{d} = \begin{bmatrix} F_\mathrm{dx} & F_\mathrm{dy} & F_\mathrm{dz} \end{bmatrix}^T$. Fig. 1 (right) shows two free body diagrams, which represent the upper and lower part of the base body with the masses $m_{\square\mathrm{o}}$ and $m_{\square\mathrm{u}}$ respectively. The separation is made by the force sensors assumed to be massless. The two equations of motion

$$m_{\square\mathrm{o}} \ddot{\vec{x}}_\square = m_{\square\mathrm{o}} \begin{bmatrix} 0 \\ 0 \\ -g \end{bmatrix} + \vec{F}_\mathrm{d} + \begin{bmatrix} F_{\parallel\mathrm{x}} \\ F_{\parallel\mathrm{y}} \\ 0 \end{bmatrix} \tag{1}$$

$$m_{\square\mathrm{u}} \ddot{\vec{x}}_\square = m_{\square\mathrm{u}} \begin{bmatrix} 0 \\ 0 \\ -g \end{bmatrix} + \vec{F} - \vec{F}_\mathrm{d} \tag{2}$$

describe the associated force equilibria. $F_{\parallel\mathrm{x}}$ and $F_{\parallel\mathrm{y}}$ are possible reaction forces in the vertical guidance. The torques $\vec{M}_\parallel$, $\vec{M}_\mathrm{d}$ and $\vec{M}$ have no influence on the relationships described below, but they are nevertheless shown in Fig. 1 (right) for the sake of completeness. As all partial bodies are rigidly connected to each other, they all have the same acceleration $\ddot{\vec{x}}_\square = \begin{bmatrix} 0 & 0 & \ddot{z}_\square \end{bmatrix}^T$. By rearranging Eq. (1) and Eq. (2), the forces acting between the base body and the counter body

$$F_\mathrm{x} = F_\mathrm{dx} \tag{3}$$

$$F_\mathrm{y} = F_\mathrm{dy} \tag{4}$$

$$F_\mathrm{z} = \left(1 + \frac{m_{\square\mathrm{u}}}{m_{\square\mathrm{o}}}\right) F_\mathrm{dz} \tag{5}$$

can be calculated as a function of the forces F_dx, F_dy and F_dz transmitted in the dynamometer. This relationship is independent of the movement $z(t)$ and applies in both static and dynamic cases at any time t. The decisive difference between the horizontal and vertical force components is the guide that prevents the horizontal movement of the weight.

The result shows that the conversion formula is determined by the ratio of the masses above and below the force sensors. For the limiting case $m_{\square\mathrm{u}} \to 0$, i. e. when the force measurement takes place directly in the tribological contact surfaces, $\vec{F} = \vec{F}_\mathrm{d}$ applies. However, if the sensor is located far away from the tribological contact surfaces, so that the mass $m_{\square\mathrm{o}} \to 0$ is very low, the factor $\left(1 + \frac{m_{\square\mathrm{u}}}{m_{\square\mathrm{o}}}\right)$ becomes infinitely large and the actual force $\vec{F}_\mathrm{z}$ in the tribological system can no longer be determined accurately. In reality, there are always measurement uncertainties, deformations and other external influences that affect the accuracy of a measurement. Therefore, the mass below the force sensors $m_{\square\mathrm{u}}$ should not be disproportionately large.

2.1.2 Drift correction

Undesirable drift can occur in force measurements, especially when measuring over longer periods of time. A force sensor can therefore display a different value at the beginning of the measurement compared to the end of the measurement when unloaded. This phenomenon occurs, for example, as a result of temperature changes, ref. Bernstein (2024).

To be able to correct such drifts in the measured values, it is sufficient to record the force signal before and after the actual measurement in the unloaded state. Shortly before and after the test (state 0 and 1), the base body above the force sensors is statically fixed so that the part below the force sensors hangs freely. The measured values can be used to determine the recorded force signals $\vec{F}_{\mathrm{d}*}(t_0)$ or $\vec{F}_{\mathrm{d}*}(t_1)$ both in state 0 at time t_0 or state 1 at time t_1. In the unloaded state, the force actually transmitted in the dynamometer is also known $\vec{F}_\mathrm{d}(t_0) = \vec{F}_\mathrm{d}(t_1) = \begin{bmatrix} 0 & 0 & -m_{\square\mathrm{u}} g \end{bmatrix}^T$. The sign depends on whether vertical tensile or compressive

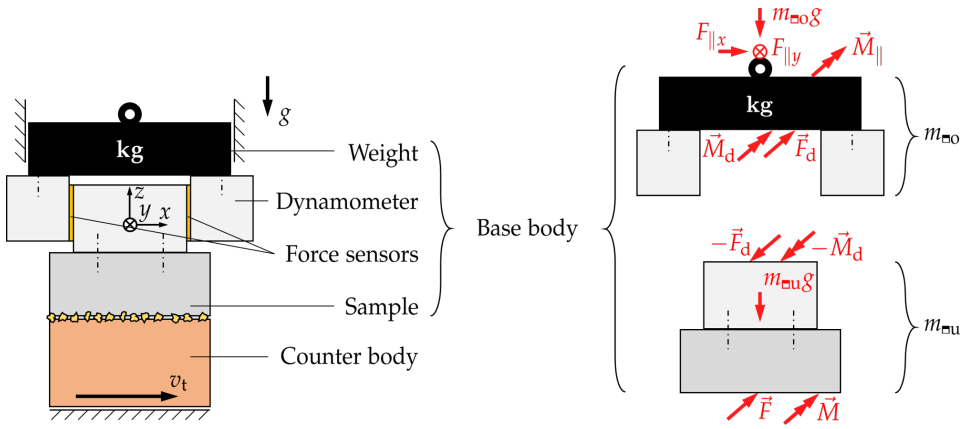

Fig. 1: Tribological three-body system with dynamometer and weight (left) and free body diagrams of the base body (right)

forces are assumed to be positive; in this example, recorded compressive forces are positive. This results in the differences

$$\Delta\vec{F}(t_0) = \vec{F}_{d*}(t_0) - \vec{F}_d(t_0) = \vec{F}_{d*}(t_0) + \begin{bmatrix} 0 \\ 0 \\ m_{\square u}g \end{bmatrix} \tag{6}$$

$$\Delta\vec{F}(t_1) = \vec{F}_{d*}(t_1) - \vec{F}_d(t_1) = \vec{F}_{d*}(t_1) + \begin{bmatrix} 0 \\ 0 \\ m_{\square u}g \end{bmatrix} \tag{7}$$

between recorded and actual forces. Assuming a linear drift for the duration of the experiment, the following applies

$$\vec{F}_d(t) = \vec{F}_{d*}(t) - \Delta\vec{F}(t) \tag{8}$$

with the time-dependent correction

$$\Delta\vec{F}(t) = \Delta\vec{F}(t_0) + \left(\Delta\vec{F}(t_1) - \Delta\vec{F}(t_0)\right) \cdot \frac{t - t_0}{t_1 - t_0} \tag{9}$$

in the time interval $\forall t \in [t_0, t_1]$. Eqs. (3)-(5) can be used to calculate the forces transmitted in the tribological contact zone

$$F_x = F_{d*x} - \Delta F_{dx} \tag{10}$$

$$F_y = F_{d*y} - \Delta F_{dy} \tag{11}$$

$$F_z = \left(1 + \frac{m_{\square u}}{m_{\square o}}\right)(F_{d*z} - \Delta F_{dz}) \tag{12}$$

as functions of the recorded force signals F_{d*x}, F_{d*y} and F_{d*z} in conjunction with correction terms ΔF_{dx}, ΔF_{dy} and ΔF_{dz}.

2.1.3 Natural vibrations

In addition, natural vibrations can occur in the system due to the finite stiffness of the force sensors, whose frequency decreases when additional weight is attached. This reduces the range in which frequencies, occurring due to processes in the tribological contact zone, can be recorded reliably and without distortion.
Assuming that the deformation of the system predominantly occurs in the force sensors and the rest of the system continues to behave rigidly, the natural frequency can be calculated for a given stiffness c of the dynamometer. An analogous system for this case is shown in Fig. 2.
There are two different cases. If the base body rests permanently on the intermediate medium or counter body, only the subsystem above the spring with (the homogeneous part of) the equation of motion

$$m_{\square o}\ddot{z}_{\square o} = -c \cdot z_{\square o} \tag{13}$$

freely oscillates. Forming provides the differential equation

$$\ddot{z}_{\square o} + \underbrace{\frac{c}{m_{\square o}}}_{=(2\pi f_1)^2} \cdot z_{\square o} = 0 \tag{14}$$

and consequently the natural frequency of the system

$$f_1 = \frac{1}{2\pi}\sqrt{\frac{c}{m_{\square o}}} \tag{15}$$

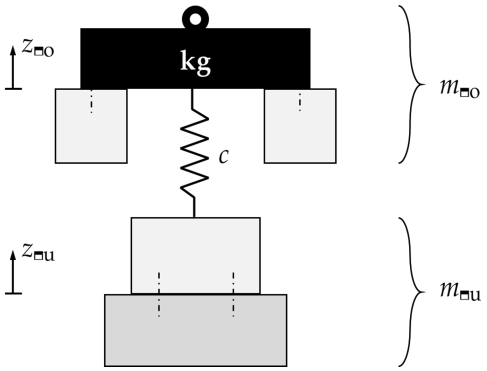

Fig. 2: Analogous system of the base body with force sensors of stiffness c

depends on the mass $m_{\square o}$ above the force sensors.
However, if the base body loses contact with the intermediate medium or counter-body, the masses above and below the spring can oscillate freely. In this case, the coupled differential equations

$$\begin{bmatrix} m_{\square o} & 0 \\ 0 & m_{\square u} \end{bmatrix} \cdot \begin{bmatrix} \ddot{z}_{\square o} \\ \ddot{z}_{\square u} \end{bmatrix} + \begin{bmatrix} c & -c \\ -c & c \end{bmatrix} \cdot \begin{bmatrix} z_{\square o} \\ z_{\square u} \end{bmatrix} = \begin{bmatrix} 0 \\ 0 \end{bmatrix} \tag{16}$$

determine the movements. The roots of the characteristic polynomial

$$\mathcal{P}(f_2) = \det\left(-(2\pi f_2)^2 \begin{bmatrix} m_{\square o} & 0 \\ 0 & m_{\square u} \end{bmatrix} + \begin{bmatrix} c & -c \\ -c & c \end{bmatrix}\right) = (2\pi f_2)^2 \cdot \left[m_{\square o} m_{\square u} (2\pi f_2)^2 - c\,(m_{\square o} + m_{\square u})\right]$$

determine the natural frequency f_2 for this system. The possible solution $f_2 = 0$ describes the collective free movement of the two masses, but is not relevant for the forces occurring in the spring. The sought natural frequency

$$f_2 = \frac{1}{2\pi}\sqrt{\frac{c}{m_{\square o}} + \frac{c}{m_{\square u}}} \tag{17}$$

depends on both the mass $m_{\square o}$ above and the mass $m_{\square u}$ below the force sensors.
Whether the frequency f_2 is actually noticeable in a system and can also be measured depends on how long and how often the base body loses contact with the intermediate medium. In addition, two extreme cases are dealt with here. In the tribological contact area, however, a finite contact stiffness must also be assumed and if a particle-fluid mixture is present as an intermediate medium, a damping effect and consequently a possible reduction of the natural frequency f_2 must also be considered.
Nevertheless, when describing the base body as an undamped two-mass oscillator, cf. Fig. 2, the relation between the force F_z in the tribological contact and the force F_{dz} transmitted in the force sensors is frequency-dependent. The coupled differential equations

$$\begin{bmatrix} m_{\square o} & 0 \\ 0 & m_{\square u} \end{bmatrix} \cdot \begin{bmatrix} \ddot{z}_{\square o} \\ \ddot{z}_{\square u} \end{bmatrix} + \begin{bmatrix} c & -c \\ -c & c \end{bmatrix} \cdot \begin{bmatrix} z_{\square o} \\ z_{\square u} \end{bmatrix} = \begin{bmatrix} 0 \\ F_z \end{bmatrix} \tag{18}$$

for a frequency-dependent excitation $F_z = \hat{F}_z \cos(2\pi f_a t)$ are satisfied by the solution

$$\begin{bmatrix} z_{\square o} \\ z_{\square u} \end{bmatrix} = \begin{bmatrix} c \\ c - m_{\square o}(2\pi f_a)^2 \end{bmatrix} \cdot \frac{\hat{F}_z \cos(2\pi f_a t)}{(2\pi f_a)^2 \cdot \left[m_{\square o} m_{\square u} (2\pi f_a)^2 - c\,(m_{\square o} + m_{\square u})\right]} \tag{19}$$

and consequently (in the steady state) the relationship

$$F_{dz} = c \cdot (z_{\square u} - z_{\square o}) = \frac{\frac{c}{m_{\square u}}}{\frac{c}{m_{\square u}} + \frac{c}{m_{\square o}} - (2\pi f_a)^2} \cdot F_z \tag{20}$$

between F_z and F_{dz} holds true. Solving for F_z returns

$$F_z = \frac{\frac{c}{m_{\square u}} + \frac{c}{m_{\square o}} - (2\pi f_a)^2}{\frac{c}{m_{\square u}}} \cdot F_{dz} \tag{21}$$

and thus a frequency-dependent conversion rule. For sufficiently low frequencies $f_a \to 0$ Eq. (5) still applies. For $f_a \to f_2$, however, $F_z = 0$, meaning these frequency components cannot be determined from the measurement data. Therefore, a low-pass filter should be applied to the recorded measurement data, for example with a cut-off frequency $f_{limit} = \frac{1}{2} f_2$, in order to exclude the frequency components that cannot be precisely determined from further evaluation of the measurement data.
In addition to the vertical oscillations considered here, bending oscillations or oscillations in x- or y-direction can also occur, whereby the dynamometer can have different stiffnesses in x-, y- and z-direction. Further investigation of the natural frequencies is not carried out in this publication. The formulas in this Sect. 2.1.3 are only used to estimate the order of magnitude of the natural frequencies to be expected and which variables have an impact on them.
The examples considered in Sect. 2.1 show that the masses and thus the selected load application method not only have an effect on the tribological system itself, but also on the measurement data and the measurability of certain phenomena. With other load application methods, other properties may have to be taken into account.

2.2 Real test stand

This section deals with the test stand, which enables the realization of tribological three-body wear systems. First, the reasoning behind the chosen test setup is explained. Secondly, the explicit design is outlined.

2.2.1 Substantiation of the selected realization

The ideal system that needs to be realized consists of a flat counter body that moves with the sliding speed v_t and an only vertically movable base body, as already described in Sect. 2.1. The intermediate medium is located between the parallel contact surfaces of the base body and the counter body.
However, there are some differences in the realization, see Fig. 3. The relative horizontal motion between the base and counter body is accomplished by rotating the counter body. As a result, the relative speed in the contact zone is location-dependent, but this allows sliding paths of any length to be investigated with small space requirement. The speed range in the tribological contact can also be small if the sample dimensions are significantly smaller than its distance from the axis of rotation of the counter body. The base body also consists of several components that allow the sample to be tilted meaning that the sample surface can always be aligned parallel to the surface of the counter body. Parallelism is important for experiments with very small particle diameters in the range of a few micrometers. For example, tilting the sample by just 0.0573° corresponds to a slope of 10 micrometers per centimeter. Given that the sample surfaces have dimensions of approx. 20 mm × 30 mm and that the alignment and axis of rotation of the counter body are subject to tolerances, it is almost inevitable that the sample will tilt in order to align the base and counter body surfaces parallel to each other. Compensation for parallelism is realized by a modified ball joint as shown in Fig. 4 (left). Rotations around the vertical axis are prevented by a pin firmly connected to the ball. To minimize friction in the joint, a solid lubricant based on polytetrafluoroethylene particles is used.
In tribological systems, there are typically tangential forces acting along the body surfaces. Fig. 4 (right) shows the sample and ball joint in cross-section. Neglecting inertia, vertical movement, friction in the ball joint and any tilting movements of the sample, it can be seen that the sample must be placed eccentrically in order to achieve a uniform load on the sample surface. If the load is evenly distributed, the resulting normal force F_n acts in the center of the sample. The tangential force F_t acts directly along the sample surface and thus at a distance $\Delta z \approx 15.5\,\text{mm}$ from the rotational center of the ball joint. Equilibrium of moments

$$0 = F_n \cdot \Delta x - F_t \cdot \Delta z \tag{22}$$

results in the relationship

$$\Delta x = \frac{F_t}{F_n} \cdot \Delta z \tag{23}$$

for the horizontal offset Δx. The ratio of tangential force and normal force corresponds to the coefficient of friction $\mu = \frac{F_t}{F_n}$ of the tribological system. The adjustment of Δx allows at least partial compensation of otherwise non-uniform loads due to tangential forces.
Further differences between the ideal system and the realization exist due to the rigid body assumption that never applies in reality. Natural vibrations are discussed in Sect. 2.1.3. Further effects caused by interfering factors such as friction in the vertical guidance of the base body, temperature fluctuations and other environmental influences cannot be completely eliminated in any of the tests.

2.2.2 Experimental arrangement

The arrangement of the base and counter body is sketched in Fig. 5. The counter body is a circular disc with a diameter of $D = 270\,\text{mm}$ and a thickness of $t = 2\,\text{mm}$, which is mounted on an adapter with four bolts to prevent torsional slip. The adapter is rotated by stepper motor 1 (ES-MH342200 from Leadshine Technology Co., Ltd.) with an intermediate transmission gear (transmission ratio 36:1). A pressed-on inner disc (material nitrile rubber) and an outer screwed-on steel ring with a silicone seal (material Ecoflex 00-30) are mounted onto the circular disc to keep particles and liquid on a track with inner radius $r_i = 80\,\text{mm}$ and outer radius $r_a = 120\,\text{mm}$.

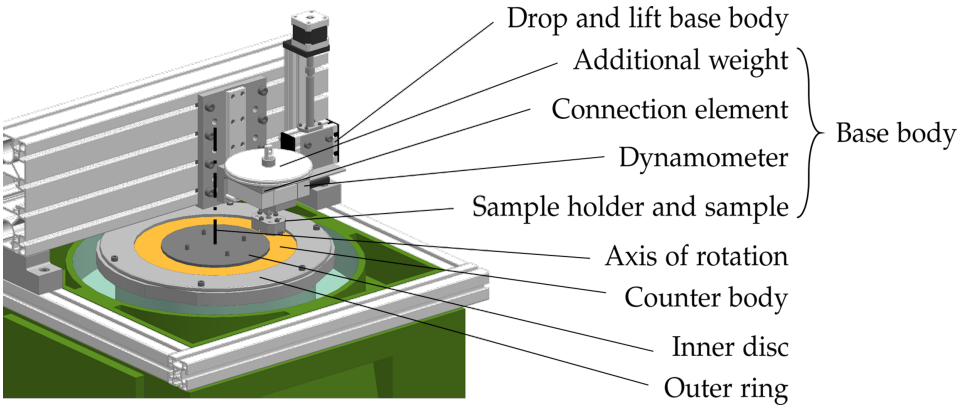

Fig. 3: CAD model of the test stand for the realization of tribological experiments

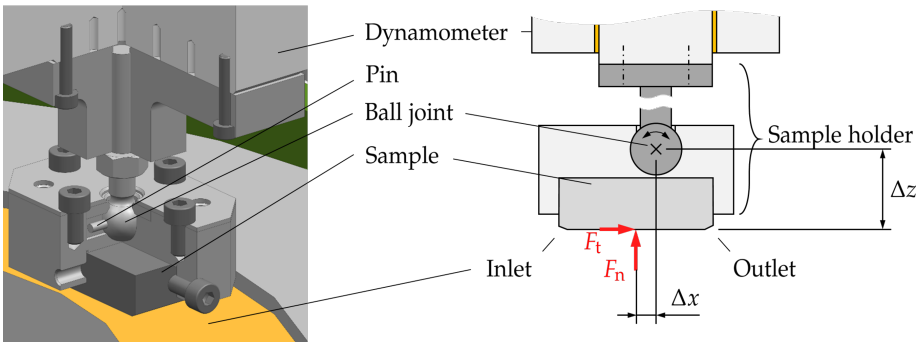

Fig. 4: CAD model of the modified ball joint in section (left) and sample and sample holder in cross-section (right)

The sample with the dimensions 20 mm × 30 mm × 10 mm with 30° × 1.2 mm chamfers at the inlet and outlet is fixed in the sample holder. The center of the sample is positioned at a distance of $r_\otimes = 100$ mm from the axis of rotation of the counter body. The sliding speed v_t between the sample center and the counter body in the tribological contact zone can be determined by the rotational speed $\omega = \frac{v_t}{r_\otimes}$. The tribological contact between the sample and the counter body takes place exclusively along the annular track onto which particles and optionally liquid are applied.
The sample holder is connected to the cover plate of the dynamometer (type 9119AA1 from Kistler Instrumente AG). A connection element connects the two base plates of the dynamometer with the vertical guide (type SHW17CA1M+175LM from THK GmbH without seals) and enables additional weights to be applied. An automated mechanism to drop and lift the base body enables tribological experiments to be carried out with a defined sliding distance; even shorter sliding distances $s < 1$ m can be set with high reproducibility. Actuation and measurement data acquisition is carried out using the chair's in-house LabVIEW software. An overview of the electronic modules used and their tasks and communication can be found in Fig. 6.

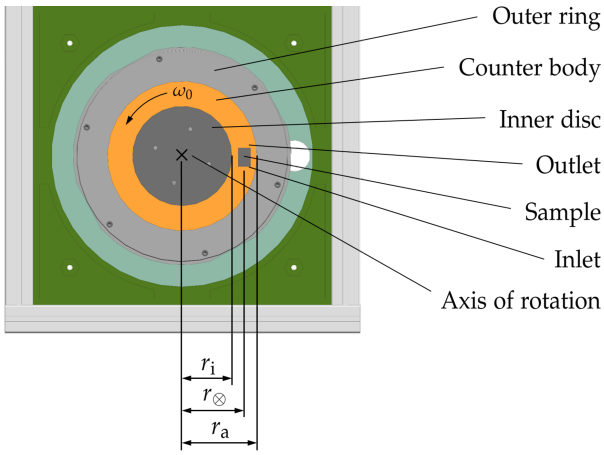

Fig. 5: Top view of CAD model of sample and counter body

2.3 Test series

The purpose of the experiments is essentially to investigate the impact of the (mean) particle diameter $\bar{d}_p$, the proportion of area covered by particles c_p (i. e. area coverage ratio), the applied load F_g and the sliding speed v_t on the tribological system. For simplified notation, instead of the physical values of the factors $\bar{d}_p$, c_p, F_g or v_t level values $\bar{d}_p^*$, c_p^*, F_g^* or v_t^* (with unit 1) are utilized. The parameter ranges and conversion rules between levels and physical quantities are explained in Sect. 2.3.4.
Tab. 1 shows a five-level *One-Factor-At-A-Time* experimental design. It comprises experiments in which a single factor is varied at a time, while all other factors remain at center level. This experimental design enables the direct representation of result variables as a function of a single factor, but the center levels of the factors are set much more often than the other levels and possible interactions between the varied factors cannot be investigated.
Tab. 2 shows a composite experimental design. Test number 0 describes the central point of the factor space. Test numbers 1b to 8b are a fractional factorial test plan of resolution IV (Siebertz et al. (2017)), where each factor is tested four times at level +1 and four times at level −1, meaning that the test plan is balanced. In addition, the factors are uncorrelated with each other, allowing the correlation between each factor and the result variables to be determined. Main effects are only confounded with triple interactions and double interactions are confounded with each other, ref. Siebertz et al. (2017). The experiment numbers 9 to 16 are used to extend the experimental design in order to identify quadratic effects.
Apart from the differences between the experiments 1a to 8a and the experiments 1b to 8b, the required experiments of the two experimental designs (Tab. 1 and Tab. 2) are identical. Both experimental designs offer advantages and a description model of the result variables determined using the composite experimental design can be verified with the experiments 1a to 8a as test points. A total of 25 different experiments are required to carry out both experimental designs.

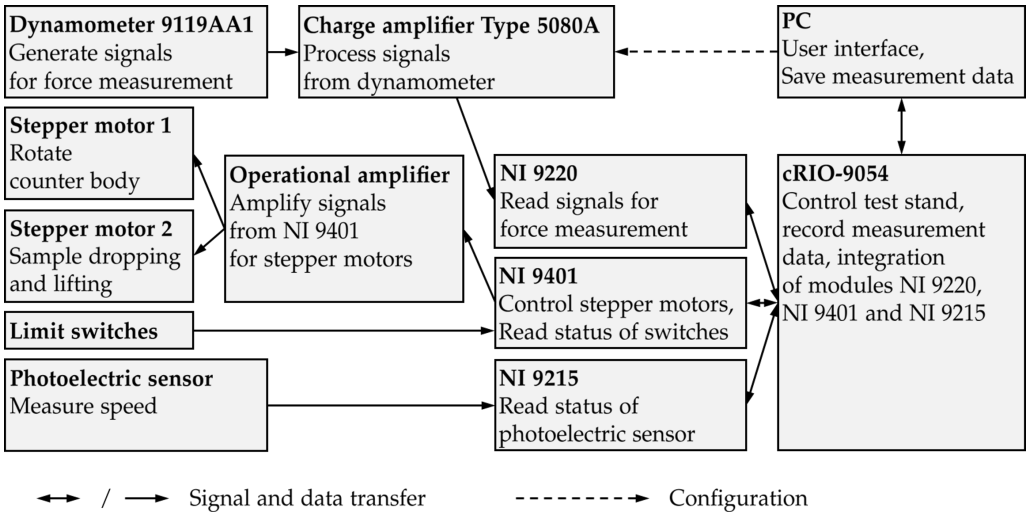

Fig. 6: Actuation of the test stand and measurement data acquisition

2.3.1 Test materials

The samples are made of case-hardened 16MnCr5, a low-alloy case-hardening steel. First, the samples are cut from a flat bar with a rectangular cross-section of 20 mm × 30 mm and milled into the geometry 30 mm × 20 mm × 10 mm minus the 1.2 mm wide 30° chamfers. They are carburized in a heat treatment process lasting several hours. The carburization process results in a carbon plateau with relatively constant hardness down to a depth of approx. 0.5 mm. Subsequently, approx. 60 µm is first removed from the back of the samples by surface grinding and then approx. 20 µm is removed from the front. On the one hand, this procedure removes the scale layer on the sample. On the other had, thermal distortion is compensated in this way and an extremely flat sample surface is achieved. The samples are then polished with polishing agents of grain size 6 µm, 3 µm and finally 1 µm in the University's in-house metal workshop before the experiments are conducted.

The counter body is a circular disc made of steel DC01. Each individual metal disc is only used for a single grain size to minimize the risk of particle carryover. A copper disc made of Cu-DHP is also used to investigate the influence of the counter body material.

The particles used in the experiments are made of black SiC (silicon carbide) of the grit sizes F 600, F 320, F 180, F 60 and F 24, with the corresponding mean particle diameters 9.30 µm, 29.20 µm, 81.00 µm, 274.00 µm and 775.00 µm, respectively. Before each individual experiment, previously unused particles of the respective grain size are weighed, applied onto the counter body and disposed of after the experiment.

Unless explicitly stated otherwise, each test is performed with lapping oil OL 20 purchased from Stähli Läpp-Technik GmbH. For this purpose, the track on the counter body is filled with an appropriate amount of liquid so that all gaps between particles, base body and counter body are filled with liquid during tribological contact to the extent possible. The filling height required for this is determined by the particle size and is therefore also treated in this context in Sect. 2.3.4. The liquid is applied to the counter body just before the particles in order to achieve a more even distribution of the particles.

Tab. 1: Five-level *One-Factor-At-A-Time* experimental design

Test number	0	1a	2a	3a	4a	5a	6a	7a	8a	9	10	11	12	13	14	15	16
Particle size $\bar{d}_p^*$	0	1	0	0	0	−1	0	0	0	2	0	0	0	−2	0	0	0
Area coverage ratio c_p^*	0	0	1	0	0	0	−1	0	0	0	2	0	0	0	−2	0	0
Load F_g^*	0	0	0	1	0	0	0	−1	0	0	0	2	0	0	0	−2	0
Speed v_t^*	0	0	0	0	1	0	0	0	−1	0	0	0	2	0	0	0	−2

Tab. 2: Individual tests of the composite experimental design consisting of central point (test number 0), fractional factorial design with resolution IV (test numbers 1b to 8b) and extension to the central composite design for investigating nonlinear behavior (test numbers 9 to 16)

Test number	0	1b	2b	3b	4b	5b	6b	7b	8b	9	10	11	12	13	14	15	16
Particle size $\bar{d}_p^*$	0	−1	−1	−1	−1	1	1	1	1	2	0	0	0	−2	0	0	0
Area coverage ratio c_p^*	0	−1	−1	1	1	−1	−1	1	1	0	2	0	0	0	−2	0	0
Load F_g^*	0	−1	1	−1	1	−1	1	−1	1	0	0	2	0	0	0	−2	0
Speed v_t^*	0	−1	1	1	−1	1	−1	−1	1	0	0	0	2	0	0	0	−2

2.3.2 Test execution

Before each test, the counter body is prepared with an orbital sander (grit size P 600), carefully cleaned and mounted on the adapter, together with the inner disc and outer ring. A sample is then mounted in the sample holder, additional weights are attached or detached and defined masses of liquid (cf. Tab. 5) and particles (cf. Tab. 6) are evenly applied to the counter body.
The following processes are triggered by starting the test routine. The signals from the force sensors are detected and recorded and stepper motor 1 starts to increase the rotational speed of the counter body. After the target rotational speed is reached, the base body is dropped down onto the rotating counter body at a dropping speed of $v_{\downarrow} = 14\,\frac{\mathrm{mm}}{\mathrm{s}}$. After the previously defined sliding distance s is reached, the automatic mechanism lifts the base body up again and the counter body reduces its rotational speed to zero. The test is finished and the measurement data is saved.
Subsequently, the sample is removed from the holder, cleaned and archived for possible subsequent investigations, e.g. of the surface topography.

2.3.3 Execution sequence

The chronological order of execution plays a role in recognizing changes of the test stand or other test conditions over time, which can result, for example, in drifts or changes in the variance of a result variable. To detect such changes, the experiments are usually randomized, meaning that the chronological order of execution is random. If the variance or the mean value of a result variable increases or decreases with the chronological order of execution, this may indicate a change of the test conditions. However, if the tests are not carried out in random order, time-dependent patterns in the result variables may be due to the order of execution and do not indicate any changes in the test conditions. (Siebertz et al. (2017))
In the planned experiments, however, a greater potential for error due to particle carryover is expected, meaning that particle residues may remain in the system after cleaning, e.g. on seals. This is a particular problem if coarse particles unintentionally interfere with a tribological experiment intended to use very fine particles. For this reason, the order in which the experiments are carried out is selected in such a way that the grain size used is always greater or equal to the grain size of the previous experiment, cf. Tab. 3.
After all 25 tests have been carried out once, all items are thoroughly cleaned and a new outer seal is inserted. This procedure is carried out a total of three times; faulty tests are repeated in the next execution if necessary. Afterwards, the central point is tested in the variants

- with Cu-DHP instead of DC01 as counter body material (with lapping oil OL 20) and
- without any oil in dry contact (with DC01 as counter body material)

to investigate the influence of the counter body material and the liquid.

Tab. 3: Execution sequence of the individual experiments listed in Tab. 1 and Tab. 2

Execution sequence	Test number	$\bar{d}_{\mathrm{p}}^{*}$	c_{p}^{*}	F_{g}^{*}	v_{T}^{*}
1	13	−2	0	0	0
2	5a	−1	0	0	0
3	1b	−1	−1	−1	−1
4	2b	−1	−1	1	1
5	3b	−1	1	−1	1
6	4b	−1	1	1	−1
7	0	0	0	0	0
8	2a	0	1	0	0
9	3a	0	0	1	0
10	4a	0	0	0	1
11	6a	0	−1	0	0
12	7a	0	0	−1	0
13	8a	0	0	0	−1
14	10	0	2	0	0
15	11	0	0	2	0
16	12	0	0	0	2
17	14	0	−2	0	0
18	15	0	0	−2	0
19	16	0	0	0	−2
20	1a	1	0	0	0
21	5b	1	−1	−1	1
22	6b	1	−1	1	−1
23	7b	1	1	−1	−1
24	8b	1	1	1	1
25	9	2	0	0	0

2.3.4 Parameter ranges and levels

The physical parameter ranges investigated and the choice of discrete physical values tested in the experiments are partly motivated by theoretical considerations and partly by practical circumstances. The physical values for the respective levels are given in Tab. 4.

Tab. 4: Physical values of the factors depending on the respective levels $\{-2, -1, 0, 1, 2\}$

Factor	Level				
	−2	−1	0	1	2
Particle size $\bar{d}_\mathrm{p}$	9.30 µm	29.20 µm	81.00 µm	274.00 µm	775.00 µm
Area coverage ratio c_p	10 %	20 %	30 %	40 %	50 %
Load F_g	20.89 N	25.79 N	30.70 N	35.60 N	40.51 N
Speed v_t	30 $\frac{\mathrm{mm}}{\mathrm{s}}$	60 $\frac{\mathrm{mm}}{\mathrm{s}}$	120 $\frac{\mathrm{mm}}{\mathrm{s}}$	210 $\frac{\mathrm{mm}}{\mathrm{s}}$	330 $\frac{\mathrm{mm}}{\mathrm{s}}$

The particles used with the grit sizes F 600, F 320, F 180, F 60 and F 24 (mean particle diameters 9.30 µm, 29.20 µm, 81.00 µm, 274.00 µm and 775.00 µm) correspond to the step values −2, −1, 0, 1 and 2, respectively. The mean grain diameters $\bar{d}_\mathrm{p}$ according to Klocke (2017) are summarized in Tab. 4. The calculation rule for the approximate determination of the mean grain diameter $\bar{d}_\mathrm{p}$ using the step values is performed using the function

$$\bar{d}_\mathrm{p}\left(\bar{d}_\mathrm{p}^*\right) = 85.69 \cdot \mathrm{e}^{1.108\,\bar{d}_\mathrm{p}^*}\ \mu\mathrm{m} \tag{24}$$

with deviations between −5.3 % and 5.8 % from the values according to Klocke (2017). Eq. 24 allows the grain size to be viewed as a continuous variable instead of a categorical variable, which in turn allows results to be estimated between the tested levels. The mass m_l of liquid to be applied is selected so that preferably no air bubbles enter the lubrication gap during the tests. Tab. 5 shows the mass m_l to be applied as a function of the mean particle diameter $\bar{d}_\mathrm{p}$.

Tab. 5: Liquid mass m_l to be applied for an experiment as a function of the mean particle diameter $\bar{d}_\mathrm{p}$

$\bar{d}_\mathrm{p}$	9.30 µm	29.20 µm	81.00 µm	274.00 µm	775.00 µm
m_l	14.53 g	15.06 g	16.45 g	21.62 g	35.04 g

While in experimental studies mass concentrations (Li et al. (2022); Dwyer-Joyce et al. (1994); Williams and Hyncica (1992b,a)) or mass fractions (Stachowiak and Stachowiak (2001)) of the particles in the particle-fluid mixtures are often used to quantify the particles in the intermediate medium, the investigations in this work are based on the area coverage ratio c_p, i. e. the proportion of the counter-body surface that is covered with particles. On the one hand, only individual particle layers are ever applied for the tests and, on the other hand, this parameter can also be set for dry tests, i. e. independently of any liquid used. The value $c_\mathrm{p} = 1$ describes a complete layer of particles covering the counter body surface without any gaps, while the value $c_\mathrm{p} = 0$ means that there is not a single particle on the counter body. The area coverage ratio

$$c_\mathrm{p}\left(c_\mathrm{p}^*\right) = \left(3 + c_\mathrm{p}^*\right) \cdot 10\,\% \tag{25}$$

assumes values between a minimum of 10 % and a maximum of 50 % in the tests. Based on Czichos and Habig (2020), the value $\bar{\rho}_\mathrm{p} = 3.1\ \frac{\mathrm{g}}{\mathrm{cm}^3}$ is assumed for the density. Tab. 6 lists the total particle masses m_p to be applied in a test depending on the mean particle diameter $\bar{d}_\mathrm{p}$ and the ratio c_p of the area covered with particles for the combinations used in this work. The masses are determined using the precision balance (PCB 250-3 from KERN & SOHN GmbH).
The external load F_g in the vertical direction is applied by weights. The dead weight of the components of the test stand ($m = 2.13$ kg) causes a vertical load in the tribological contact area, which corresponds to the level $F_\mathrm{g}^* = -2$. Additional weights in the form of discs with a mass of 500 g each can be added to the base body to realize the remaining levels −1, 0, 1 and 2. The applied load $F_\mathrm{g} = m_\square \cdot g$ is calculated using the mass $m_\square$ of the base body, which depends on the step value, and the gravitational

Tab. 6: Total particle mass m_p to be applied for an experiment depending on the mean particle diameter $\bar{d}_\mathrm{p}$ and the ratio c_p of the area covered with particles

$\bar{d}_\mathrm{p}$	c_p				
	10 %	20 %	30 %	40 %	50 %
9.30 µm	–	–	0.145 g	–	–
29.20 µm	–	0.303 g	0.455 g	0.607 g	–
81.00 µm	0.421 g	0.841 g	1.262 g	1.683 g	2.104 g
274.00 µm	–	2.846 g	4.270 g	5.693 g	–
775.00 µm	–	–	12.076 g	–	–

acceleration $g = 9.81\ \frac{\mathrm{m}}{\mathrm{s}^2}$ (Hering and Schönfelder (2023)). The load

$$F_\mathrm{g}\left(F_\mathrm{g}^*\right) = (30.6979 + 4.9050\,F_\mathrm{g}^*)\,\mathrm{N} \tag{26}$$

depends linearly on the level F_g^*.
The sliding speed v_t under the center of the sample is achieved by rotating the counter body with the angular velocity $\omega = \frac{v_\mathrm{t}}{r_\otimes}$. By using the quadratic conversion rule

$$v_\mathrm{t}\left(v_\mathrm{t}^*\right) = \left(15\,\left(v_\mathrm{t}^*\right)^2 + 75\,v_\mathrm{t}^* + 120\right)\,\frac{\mathrm{mm}}{\mathrm{s}} \tag{27}$$

between the physical quantity v_t and the corresponding step value v_t^*, a finer resolution of v_t is achieved in the low speed range.
To ensure that the tribological system remains as unchanged as possible during the test duration, the sliding distance

$$s = 2\pi r_\otimes \approx 628.32\,\mathrm{mm} \tag{28}$$

is defined in all tests so that the counter body performs exactly one revolution during the contact duration. All experiments are carried out in the ambient medium of air and at room temperature. Except for the variants of the central point to investigate the influence of the counter body material and the liquid, each test is performed using liquid (i. e. lapping oil OL 20) and metal discs made of DC01 as counter body material.

3 Results and discussion

In preliminary tests, it was verified that the sliding distance, sliding speed and normal force can be set with sufficient accuracy in the tribological experiments. In addition, the value $\Delta x = 3.20\,\mathrm{mm}$ was used to adjust the sample holder based on preliminary tests, which enables a uniform normal force distribution for a coefficient of friction $\mu \approx 0.206$, cp. Fig. 4.
Sect. 3.1 provides a brief insight into the force measurement data, phenomena during dropping and lifting and provides information on the preparation of the measurement data such as the time window considered or the low-pass filtering applied. The forces are first examined in terms of relative spread (cf. Sect. 3.2) and coefficient of friction (cf. Sect. 3.3). Based on this, Sect. 3.4 deals with modeling and Sect. 3.5 deals with the topographies resulting as a consequence of the tribological experiments. Sect. 3.6 is dedicated to the influence of the counter body material and the liquid and Sect. 3.7 addresses the influence of the test execution sequence.

3.1 Brief insight into the force data

The forces occurring in the tribological system are shown for different particle sizes (test numbers 13, 0 and 9) in Fig. 7. The variance of the forces increases sharply with increasing particle size, as can be seen from the force curve, so that particularly for larger particles the range includes normal forces of $F_\mathrm{n} \approx 0$. On the one hand, this is due to the gap height variation caused by the rolling particles, which grows with increasing particle diameter. On the other hand, the liquid transmits greater forces at lower gap heights, as the liquid not only has a greater load-carrying effect at lower gap heights, but also provides greater damping of vertical movements. This can already be seen during the dropping (cf. Fig 7 second row) or lifting (cf. Fig 7 third row) of the sample. For the smallest particle size, compared to the other particle sizes, immediately after the sample is dropped (black dashed line) a significantly delayed increase in the tangential force is observed (up to the black dotted line) before it reaches an almost stationary level. This observation supports the assumption that liquid must first be squeezed out of the contact zone before the low gap heights are reached at which the particles come into contact with the sample surface. When the sample is lifted, meaning when the tribological contact is released, negative normal forces occur for a short period of time, which is also most pronounced at the smallest particle size. As the particle size increases, the intensity of these two effects decreases until it can hardly be detected with the largest particles tested.
The following two sections evaluate the standard deviations and mean values of the forces during the contact duration in order to calculate the relative spread of the forces and the coefficient of friction. For the calculation of these values, the time window to be evaluated is reduced by 0.05 s at the beginning and 0.05 s at the end of the automatically determined contact duration in order to exclude possible influences caused by the dropping and lifting events. For the grit size F 600, there is also a time window excluded from the evaluation in which the tangential force F_t has not yet reached the stationary level.
All force measurement data is processed using a low-pass filter before evaluation in order to minimize the influence of natural oscillations of the force measurement system on the measured force data. Indicative values for the lowest natural frequencies of vertical vibrations are provided in Tab. 7, for the derivation of the calculation formulas see Sect. 2.1.3. Using the internal Matlab function `filtfilt`, all force measurement data is filtered with a Butterworth filter of 6th order with the cut-off frequency $f_\mathrm{c} = 1\,\mathrm{kHz}$.

Tab. 7: Natural frequencies according to Eq. (15) and Eq. (17) for different loads F_g^*

Load F_g^*	−2	−1	0	1	2
f_1	2.85 kHz	2.46 kHz	2.22 kHz	2.00 kHz	1.85 kHz
f_2	5.11 kHz	4.91 kHz	4.78 kHz	4.70 kHz	4.64 kHz

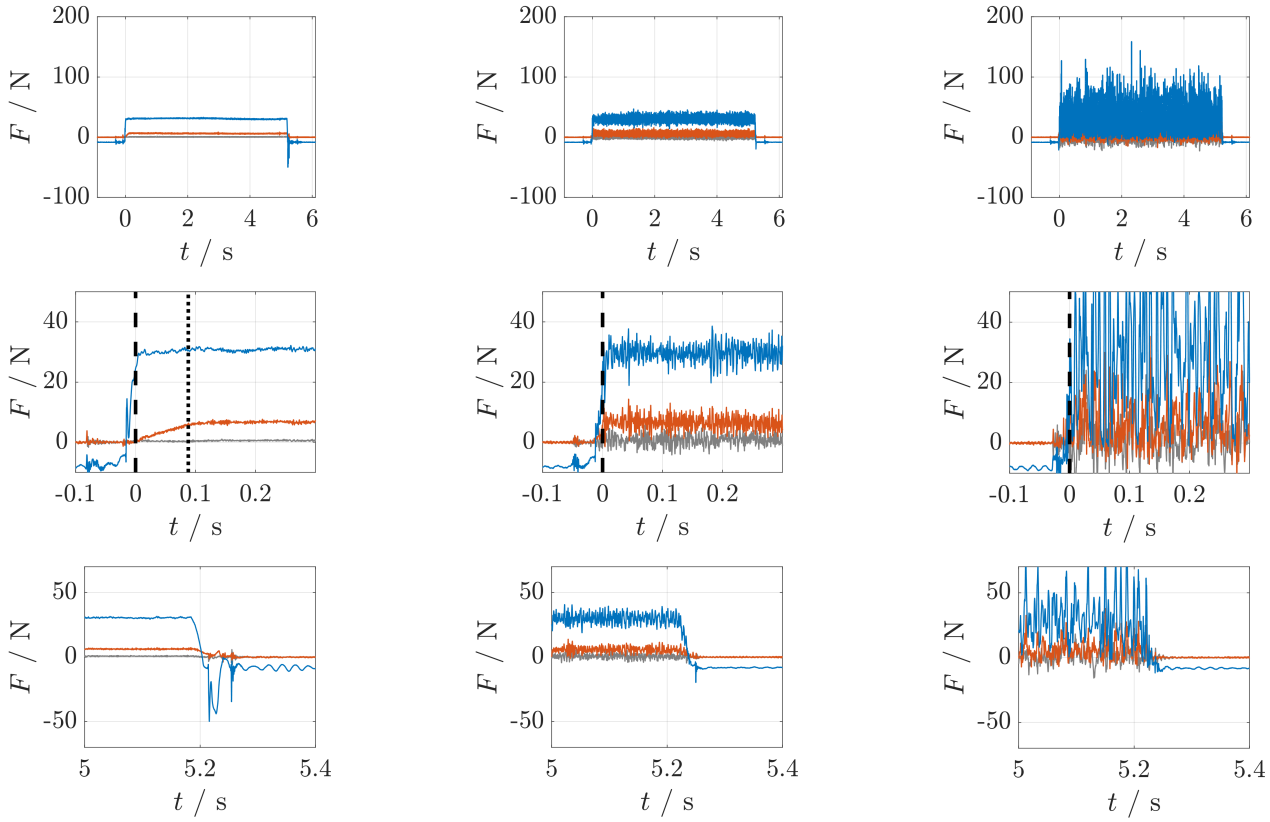

Fig. 7: Normal force F_n (blue), tangential force F_t (red) and side force F_Q (gray) as a function of time for different particle sizes F 600, F 180 and F 24 (from left to right); entire contact duration (top), dropping (middle), lifting (bottom)

3.2 Relative spread of forces

The standard deviation Std (F) of force F during the contact duration is determined to quantify the spread of the occurring forces. The standard deviation Std (ϵ) due to disturbance ϵ, determined from time periods of the force signal before dropping and after lifting the sample, have comparatively low values of maximum 0.02 N and 0.06 N for the tangential and normal force, respectively. Therefore, Std $(F) \approx$ Std $(F + \epsilon)$ is evaluated as a proxy.

Fig. 8 visualizes the relative spread (i. e. standard deviation per mean value) of the normal force $\kappa\,(F_n)$ and the relative spread of the tangential force $\kappa\,(F_t)$ as a function of the factors $\bar{d}_p^*$, c_p^*, F_g^* and v_t^*. The three runs of the experiments, each with the same factor combinations, are marked by a circle, square and triangle and demonstrate a high repeatability of the results. Fig. 9 shows half-violin plots in which the estimated probability density functions of the occurring normal forces F_n during contact are shown as a function of the factors $\bar{d}_p^*$, c_p^*, F_g^* and v_t^*. The circles mark the time-weighted mean values.

The relative spread increases with increasing particle size. In the range $\bar{d}_p^* \leq 1$ the relationship is even progressive. The representation of the normal forces in half-violin plots provides further insight into the dynamics of the tribological systems. The particle size $\bar{d}_p^*$ shows the strongest influence, from a very narrow distribution for small particle sizes to a broader distribution of the normal forces for large particles. For $\bar{d}_p^* \geq 1$ the normal forces assume values in the range $F_n \approx 0$ and for $\bar{d}_p^* = 2$ the normal force distribution is already clearly skewed. Such a skewed normal force distribution can be explained by an intermittent contact between sample and particles, which occurs for sufficiently high speeds v_t and depends on various system properties, see the previous publication of the authors Bilz and de Payrebrune (2021). For lower gap heights the liquid damps vertical movements much stronger and the movement amplitudes of the base body due to the orientation-dependent particle height are also lower for lower particle sizes. Furthermore, the movement of an erecting particle is only partially transferred to the entire base body, as the sample can tilt in the experiment. In addition, there are deformations, especially directly in the contact zone, which may suppress the occurrence of intermittent contact for small particles, cf. Bilz and de Payrebrune (2021). As the particle size decreases (while the sliding speed remains constant), the rotational speed of a rolling particle also increases. Therefore, the excitation frequency is higher. In order to confirm intermittent contact, the sampling rate of the measured forces and the lowest natural frequency of the force measuring system (see Tab. 7) must be significantly higher than the excitation frequency. Consequently, there are higher requirements for detecting intermittent contact with small particle sizes, if it occurs at all. The negative forces can also be explained by the liquid in the contact gap as well as possible natural oscillations of the experimental setup.

The influences of the remaining factors are less prominent. Both with increasing area coverage ratio c_p and with increasing load F_g, $\kappa\,(F_n)$ and $\kappa\,(F_t)$ decrease, cf. Fig. 8. The decreasing relative spread as a function of increasing load F_g is mainly due to the fact that the spread $\sigma_{\mathrm{Std,F}}$ is related to a larger mean value, cf. Fig. 9.

While the relative spread $\kappa\,(F_n)$ and $\kappa\,(F_t)$ correlate strongly depending on the factors $\bar{d}_p$, c_p and F_g, the correlation as a function of the sliding speed v_t is only maintained for low sliding speeds. For low sliding speeds, $\kappa\,(F_n)$ and $\kappa\,(F_t)$ increase as the sliding speed increases, whereas for higher sliding speeds only $\kappa\,(F_n)$ increases further, $\kappa\,(F_t)$ on the other hand decreases slightly. One

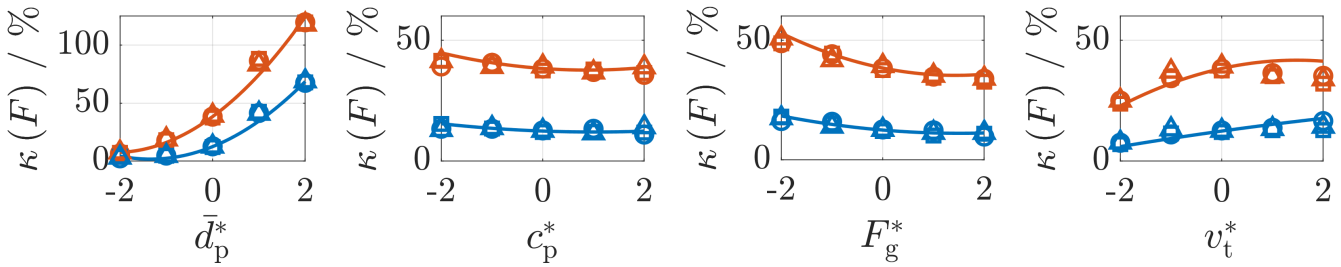

Fig. 8: Relative spread $\kappa(F_n)$ (blue) and $\kappa(F_t)$ (red) as a function of the factors $\bar{d}_p^*$, c_p^*, F_g^* and v_t^*; representation of the first, second or third run of the tests by circles, squares and triangles respectively

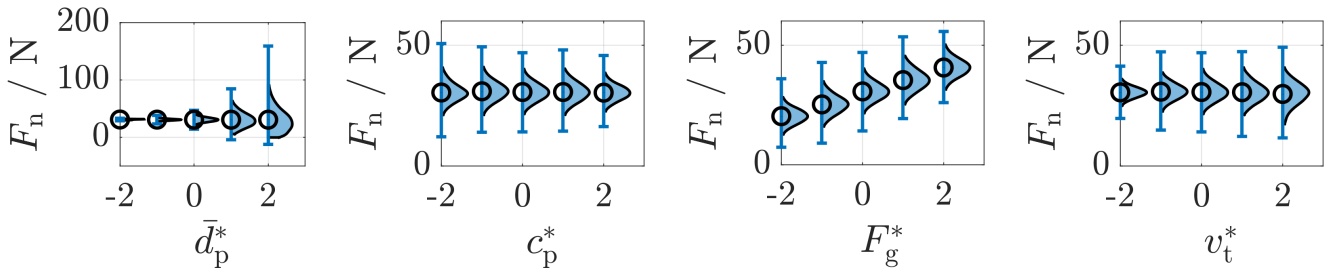

Fig. 9: Half-violin plots of the occurring normal forces F_n during the contact duration as a function of the factors $\bar{d}_p^*$, c_p^*, F_g^* and v_t^*; depiction of the first test execution

possible explanation for this opposing tendency is an increasing resistance to the rolling motion of individual particles due to the displacement and deformation of the surrounding viscous medium, whose resistance often increases even progressively with increasing deformation speed. Sliding particles could cause a more uniform tangential force and thus a reduction of $\kappa(F_t)$. At the same time, with predominantly rolling particles, no significant influence of some sliding particles on $\kappa(F_n)$ can be expected.

3.3 Coefficient of friction of the tribological systems

Fig. 10 shows the coefficient of friction $\bar{\mu} = \frac{\bar{F}_t}{\bar{F}_n}$ as a function of the levels of the *One-Factor-At-A-Time* experimental design (see Tab. 1). The coefficient of friction is within a relatively narrow interval for all tests performed. The scatter in comparison to the effects due to a factor change is significantly greater for the coefficient of friction $\bar{\mu}$ than for $\kappa(F_n)$ and $\kappa(F_t)$. Nevertheless, the particle size has a clear influence on the coefficient of friction. The influence of the other factors is significantly lower. For this reason, a different diagram range is shown for the dependencies of c_p^*, F_g^* and v_t^* than for the dependency of $\bar{d}_p^*$.
The coefficient of friction of the tribological system initially decreases with increasing particle size, reaches a minimum for the second finest grit size F 320 and then increases approximately linearly with increasing levels $\bar{d}_p^*$. The significantly higher coefficient of friction when using the grit size F 600 ($\bar{d}_p = 9.30\,\mu m$) compared to the slightly coarser grit size F 320 ($\bar{d}_p = 29.20\,\mu m$) is possibly an indication that smaller particles can become trapped in surface deepenings along the sample or counter body surface, while such deepenings are not sufficient for larger particles. The surrounding liquid also increases drag when the particle size is small. If the sliding speed remains constant, the rotational speed of rolling particles increases as the particle size decreases. For a certain area coverage ratio c_p, significantly more small particles are required than large particles. As the particle size decreases, the number of particles n_p increases and consequently the mechanical power required to deform the liquid increases considerably. In fact, the grain size F 600 causes significantly more grooves than the coarser grain sizes, cf. Sect. 3.5. The increase in the coefficient of friction with particle size in the range $-1 \leq \bar{d}_p^* \leq 2$ can possibly be explained by the associated decrease in the number of particles n_p in contact, which causes deeper indentations of the particles into the body surfaces due to higher individual particle forces. This hypothesis is supported by the following idea. Apart from the differences in size, the particle shape of the different grit sizes is relatively constant and, in particular for deeper indentations, for the cross-sectional area ΔA_p of a single contact, the following applies $\Delta A_p \propto \Delta z^{\phi}$ with $\phi < 2$. Assuming the relationships $\bar{F}_p \propto \Delta A_p$ for the mean individual particle force $\bar{F}_p$ (for plastic contact, see Czichos and Habig (2020)), and $\bar{F}_p \propto \frac{1}{n_p} \propto \bar{d}_p^2$, it follows

$$\Delta z \propto \bar{d}_p^{\frac{2}{\phi}} \quad \text{resp.} \quad \frac{\Delta z}{\bar{d}_p} \propto \bar{d}_p^{\phi^*} \quad \text{with } \phi^* > 0 \tag{29}$$

and consequently the relative penetration depth (in relation to the particle diameter) as well as the rolling resistance increases.
An increasing area coverage ratio initially causes a decrease in the coefficient of friction until it reaches a local minimum and then increases again slightly. The negative correlation in the range $c_p \leq 0$ can be explained by the decreasing penetration depths of the individual particles, while the positive correlation in the range $c_p \geq 0$ indicates increased interactions between individual particles, which interfere with each other's rolling motion. The positive correlation of the coefficient of friction with load can also be explained by the increased rolling resistance of the particles with increasing penetration depth into the body surfaces.
The sliding speed shows a slightly lower coefficient of friction for $v_t^* = -2$ than for higher sliding speeds. However, in the range $-1 \leq v_t^* \leq 2$ no clear tendency can be determined.

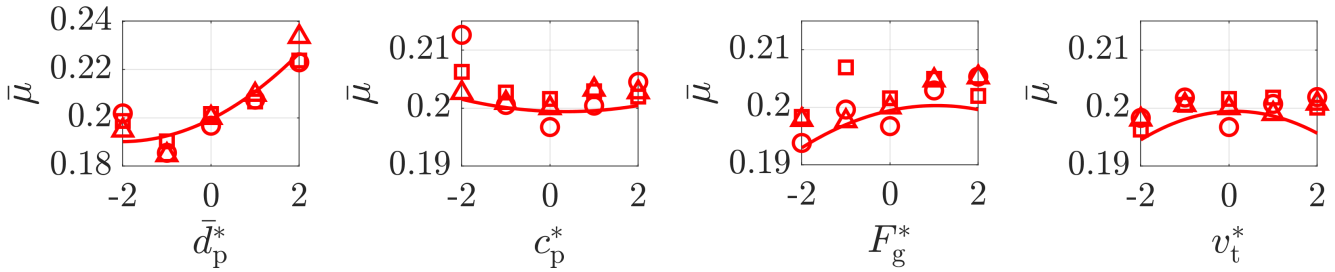

Fig. 10: Coefficient of friction $\bar{\mu}$ as a function of the factors $\bar{d}_\mathrm{p}^*$, c_p^*, F_g^* and v_t^*; representation of the first, second and third experiments by circles, squares and triangles respectively

3.4 Estimation models

Using the composite experimental design (see Tab. 2), quadratic estimation models for the result variables $\kappa\,(F_\mathrm{n})$, $\kappa\,(F_\mathrm{t})$ and $\bar{\mu}$ can be determined as a function of the factors. The estimation model

$$Y_\mathrm{exp}\left(\bar{d}_\mathrm{p}^*, c_\mathrm{p}^*, F_\mathrm{g}^*, v_\mathrm{t}^*\right) = c_0 + c_1 \cdot \bar{d}_\mathrm{p}^* + c_2 \cdot c_\mathrm{p}^* + c_3 \cdot F_\mathrm{g}^* + c_4 \cdot v_\mathrm{t}^* + c_5 \cdot \left(\bar{d}_\mathrm{p}^*\right)^2 + c_6 \cdot \left(c_\mathrm{p}^*\right)^2 + c_7 \cdot \left(F_\mathrm{g}^*\right)^2 + c_8 \cdot \left(v_\mathrm{t}^*\right)^2$$

with the nine coefficients c_0 to c_8 does not take into account any interaction effects, as these are partially confounded in the experimental design used.
Figures 8 and 10 show the predictions of the respective models as solid lines. The models largely coincide with the measured values of the *One-Factor-At-A-Time* experimental design, but limitations of the quadratic description model also become clear. For $\bar{\mu}$ and $\kappa\,(F_\mathrm{t})$ in particular, there are deviations from the trends of the measured values at high sliding speeds. The clear minimum of the coefficient of friction $\bar{\mu}$ at $\bar{d}_\mathrm{p}^* = -1$ is also not described appropriately by the quadratic model. The measured values are not perfectly reproduced by the models, but the tendencies are mostly correct. Fig. 11 compares the model predictions with the measurement results. This illustration shows that the description models used for $\kappa\,(F_\mathrm{n})$ and $\kappa\,(F_\mathrm{t})$ are quite suitable; $\bar{\mu}$, on the other hand, is described less accurately.

3.5 Resulting topography

This section discusses the resulting topography of the sample surfaces as a consequence of the tribological experiments. For this purpose, topographies are measured based on the confocal technique using a µsurf expert (from the manufacturer NanoFocus AG). All samples are polished before the tribological experiments. Any differences from this originally very flat and smooth surface topography are therefore caused by the tribological test.
Fig. 12 shows sections of the topography of three different sample surfaces including a color legend, which is valid for all topographies shown in this section. The three sample surfaces shown correspond to the three runs of test number 0. All three samples show numerous indentations scattered over the surface, as already observed (depending on the test parameters) in other studies of tribological systems with hard particles, ref. Williams and Hyncica (1992b,a); Dwyer-Joyce et al. (1994); Li et al. (2022). In addition to the indentations, there are also some scratches. The third test in particular shows a very pronounced scratch (in contrast to the first two). In this respect, the three topographies shown demonstrate visible differences, despite the fact that the input variables $\bar{d}_\mathrm{p}^*$, c_p^*, F_g^* and v_t^* of the tribological tests are the same. This can be caused, for example, by a location-dependent gap height or particle quantity or natural fluctuations in the particle properties. Regardless of the reason for the observed differences, it is clear that individual scratches can occur within the framework of natural scattering and is not sufficient in itself to prove a trend. Other, clear trends are discussed below.
As the particle size increases, the number of indentations per area decreases sharply, while the spatial dimensions of the indentations tend to increase. This can be seen on the one hand in the greatly enlarged sections in Fig. 13 and on the other hand in the less

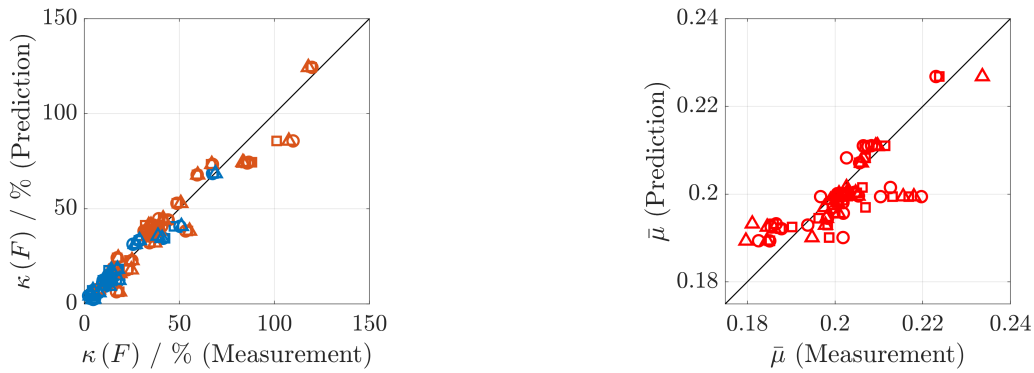

Fig. 11: Visualization of the model predictions over the measured values for the relative spread $\kappa\,(F_\mathrm{n})$ in blue and $\kappa\,(F_\mathrm{t})$ in red (left) and the coefficient of friction $\bar{\mu}$ (right)

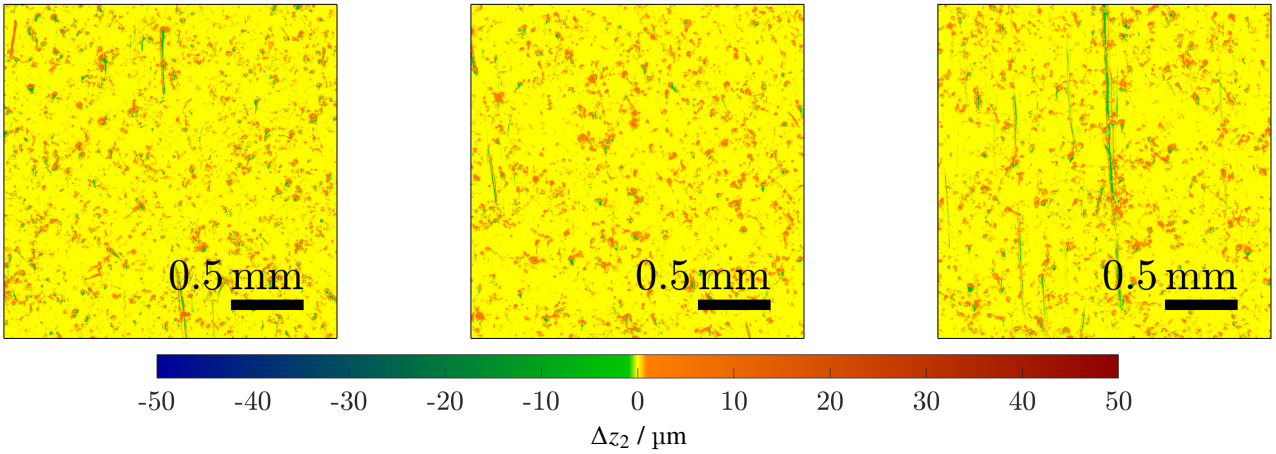

Fig. 12: Topography of the sample surface, location: middle, particle movement direction from bottom to top, first (left), second (center) and third execution of the test number 0 (right)

greatly enlarged sections in Fig. 14. For the finest grit size F 600, the sample shows many grooves running through the entire topography section. Significantly fewer and shorter grooves can already be seen for the very next coarser grit size F 320. The grit size F 24 leaves practically no grooves in the considered section at all. For the two grit sizes F 60 and F 24 in particular, it can be observed that the pile-ups preferentially occur with an offset from the indentations following the direction of particle movement.

For a low particle area coverage ratio, the sample surface shows some grooves, which are typically caused by individual particles pressed deep into the counter body surface, cf. Fig. 15. Although the coefficient of friction for $c_\mathrm{p}^* = 2$ is slightly higher than for $c_\mathrm{p}^* = 0$, only a few, not very pronounced scratches can be seen here. The particles therefore do not tend to prevent each other from rolling (even with 50 % area coverage ratio). The increased frictional resistance is therefore possibly the result of an only moderately increased rolling resistance due to higher deformation velocities of the liquid caused by smaller distances between the particles when increasing c_p. While c_p has no clear influence on the number of indentations observed here, the influence for F_g is all the clearer, see Fig. 16. An increasing load F_g causes an increase in the number of indentations in the sample surface. Even with direct contact between two rough surfaces, models predict an increase in the number of microcontacts due to an increase in load, cf. Czichos and Habig (2020). The lack of influence of c_p on the number of indentations is therefore explained by the cancellation of two opposing effects: On the one hand, a reduction in c_p causes an increase in the average load per particle, resulting in slightly deeper indentations, but this does not result in more particles penetrating the sample surface, as there are now correspondingly fewer particles in the contact gap. A change in c_p therefore does not distribute the total load to more or fewer particles, but to different subsets of particles in the gap.

The sliding speed shows no clear tendency in the range of values considered, cf. Fig. 17. However, the existing scratches for $v_\mathrm{t}^* = 2$ support the hypothesis of an increasing rolling resistance of individual particles with increasing speed due to the surrounding viscous medium, cf. Sect. 3.2. In contrast, Li et al. (2022) observes an exactly opposite trend, namely the formation of grooves at low sliding speeds v_t compared to indentations at higher speeds v_t. However, the experiments are not directly comparable, as Li et al. (2022) uses significantly smaller particles with diameters in the order of magnitude of the hydrodynamic lubrication gap height, so that the lubricating film thickness increases with the speed. In the considered case of Li et al. (2022), an increase in the sliding speed results in correspondingly reduced indentation depths of the particles and thus reduced rolling resistance.

3.6 Influence of counter body material and liquid

The central point (test number 0) is also varied to investigate the effect of the change in the counter body material, meaning that a metal disc made of Cu-DHP is used (test number $0_\mathrm{Cu-DHP}$). In another experiment, a metal disc made of DC01, but no liquid is used (test number 0_dry).

The copper material Cu-DHP used here is slightly softer than the steel DC01. Fig. 19 shows that the spatial extent of the indentations in the sample surface is smaller when the softer Cu-DHP is used as the counter body material. Particles therefore penetrate deeper into the Cu-DHP counter body surface and slightly less deeply into the sample surface under the same load, because the total load is distributed more evenly over the particles in the contact gap. On the one hand, this causes an increased rolling resistance of the particles and thus a higher coefficient of friction of the tribological system. On the other hand, erecting particles cause less pronounced gap height changes and consequently a lower variance of the normal and tangential forces, cf. Fig. 18.

Without liquid, which means with only particles in the contact gap, the damping effect of the liquid is eliminated. Therefore, larger relative spread of the forces are observed, which is also visible in the half-violin plot. The resulting topography of test number 0_dry also shows slightly larger contiguous deformed areas compared to test number 0, cf. Fig. 19. The coefficient of friction $\bar{\mu}$ is significantly higher in the dry tribological system. This can have various causes, for example capillary forces due to very small amounts of liquid in the individual contacts in a gaseous environment.

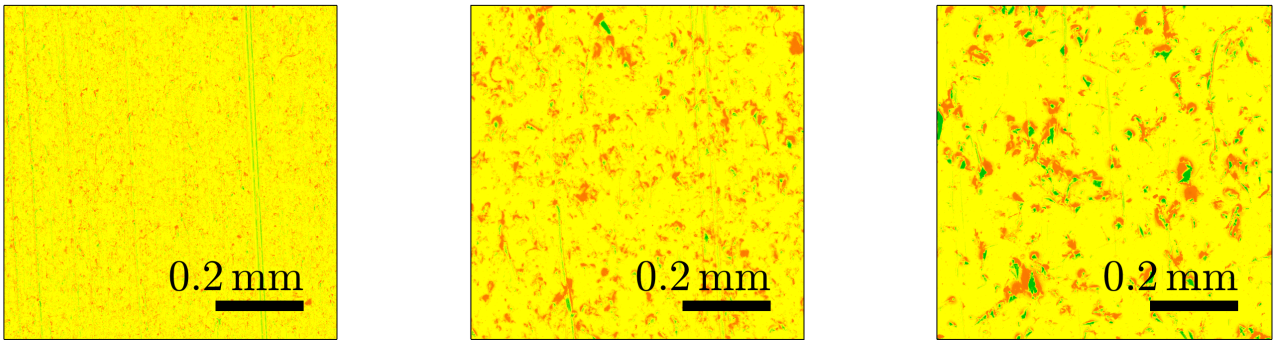

Fig. 13: Topography of the sample surface, location: middle, particle movement direction from bottom to top, grit size F 600 (left), F 320 (center) and F 180 (right)

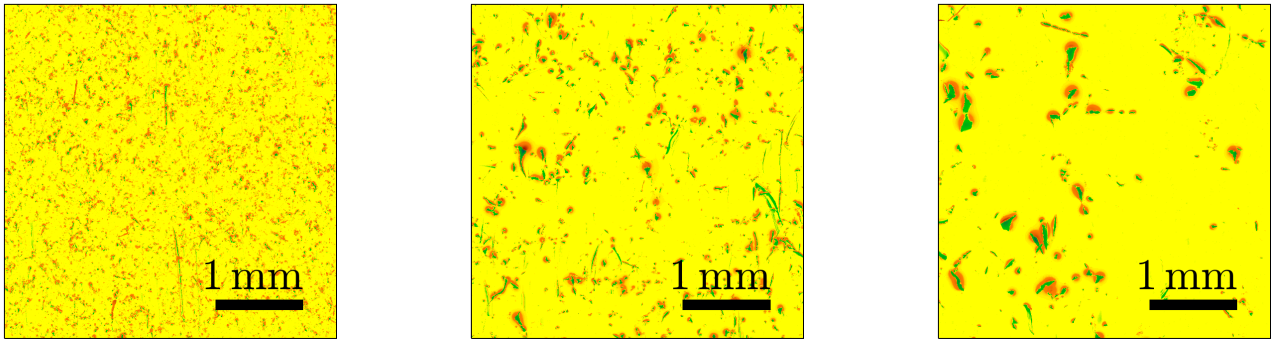

Fig. 14: Topography of the sample surface, location: middle, particle movement direction from bottom to top, grit size F 180 (left), F 60 (center) and F 24 (right)

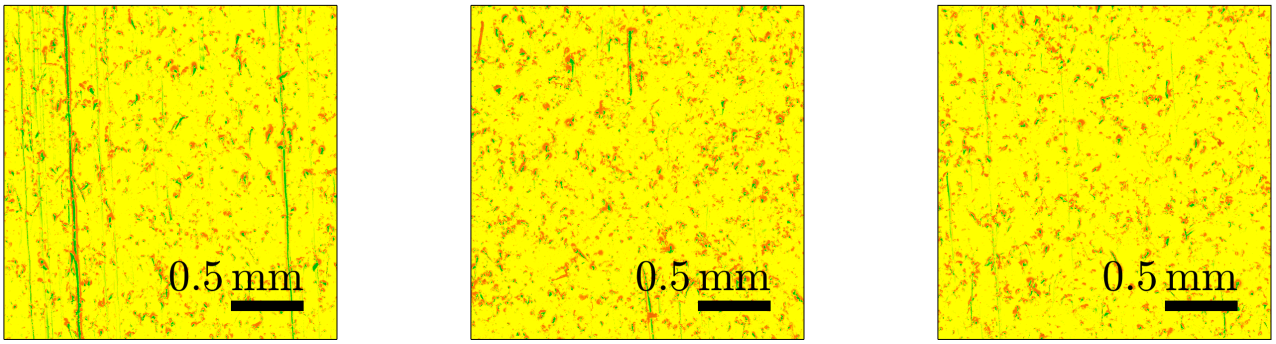

Fig. 15: Topography of the sample surface, location: middle, particle movement direction from bottom to top, area coverage ratio $c_\mathrm{p}^* = -2$ (left), $c_\mathrm{p}^* = 0$ (center) and $c_\mathrm{p}^* = 2$ (right)

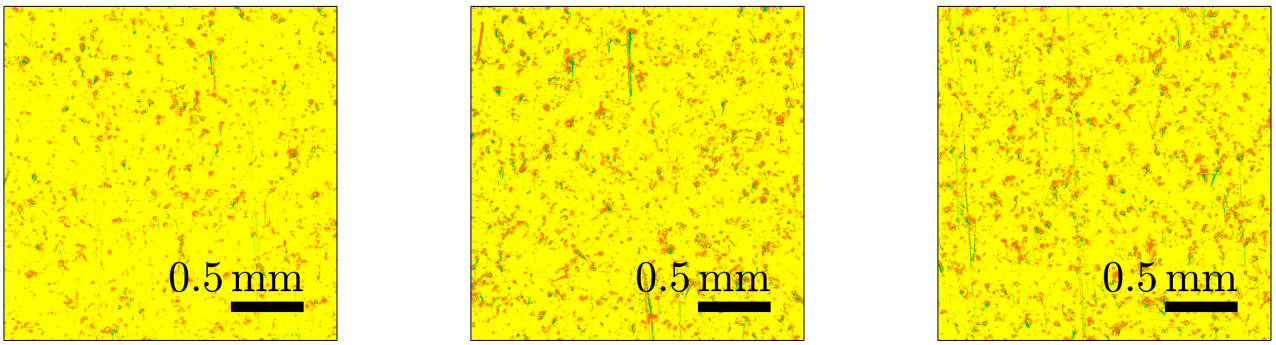

Fig. 16: Topography of the sample surface, location: middle, particle movement direction from bottom to top, load $F_\mathrm{g}^* = -2$ (left), $F_\mathrm{g}^* = 0$ (center) and $F_\mathrm{g}^* = 2$ (right)

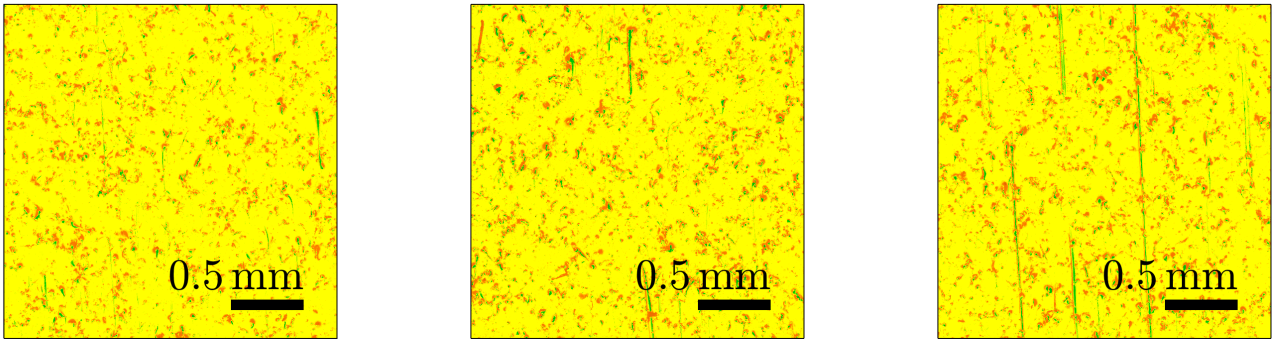

Fig. 17: Topography of the sample surface, location: middle, particle movement direction from bottom to top, speed $v_t^* = -2$ (left), $v_t^* = 0$ (center), $v_t^* = 2$ (right)

3.7 Influence of the execution sequence

One aspect that has not yet been considered is the influence of the execution sequence on the results. As already mentioned, the experiments here are not carried out in random order but with increasing particle size to avoid interference of the experiments due to particle carryover. Nevertheless, it is possible to investigate the influence of the order of execution on the experimental results. It is assumed that the scattering sequence is equally distributed if the execution sequence has no influence on a result variable.

There are six different options for the scattering order, which are shown for each of the three result variables in a separate diagram, see Fig. 20. The 27 experiments naturally show deviations from the ideal uniform distribution, if only because $\frac{27}{6}$ is not an integer. However, Pearson's chi-square statistics (Backhaus et al. (2023)) – especially with Yates's correction (Backhaus et al. (2023); Yates (1934)) for small sample sizes – make it possible to estimate the probability of being wrong about the hypothesis that the deviations from the uniform distribution are not purely random, but systematic in nature. The probabilities of being wrong (using the Yates correction) are 99.89 %, 40.25 % and 87.90 % that the scattering sequence of the result variables $\kappa\,(F_n)$, $\kappa\,(F_t)$ and $\bar{\mu}$ is not purely random.

This approach does not prove that the order of implementation has no influence on the results. However, if the relative frequencies had deviated significantly from the uniform distribution, it would have been possible to prove the opposite. Since this is not the case, the influence of the execution sequence on the result variables under consideration (even if present) is found to be insignificant and therefore negligible.

In particular for the outcome variables $\kappa\,(F_n)$ and $\kappa\,(F_t)$, the scatter is very small compared to the observed effect size anyway. A slight dependence on the order of implementation is therefore not necessarily a problem.

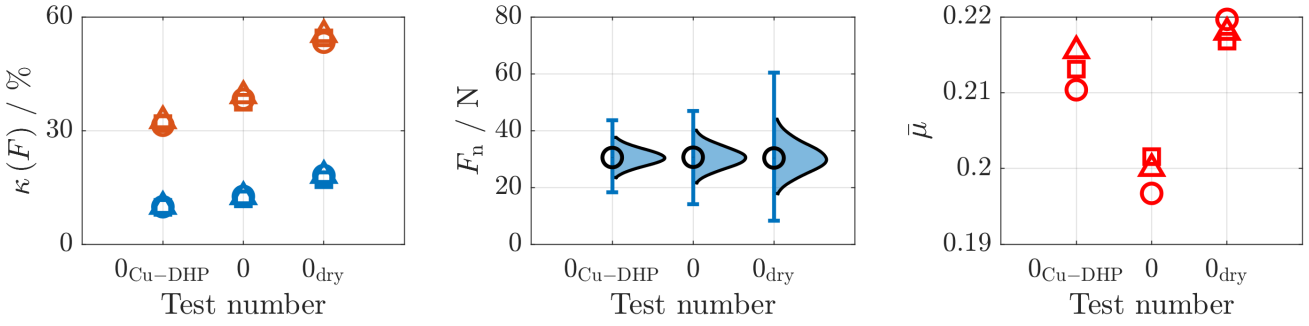

Fig. 18: Impact on the result variables $\kappa\,(F_n)$ in blue and $\kappa\,(F_t)$ in red (left), the normal force distribution as half-violin plots (center) and the coefficient of friction $\bar{\mu}$ (right)

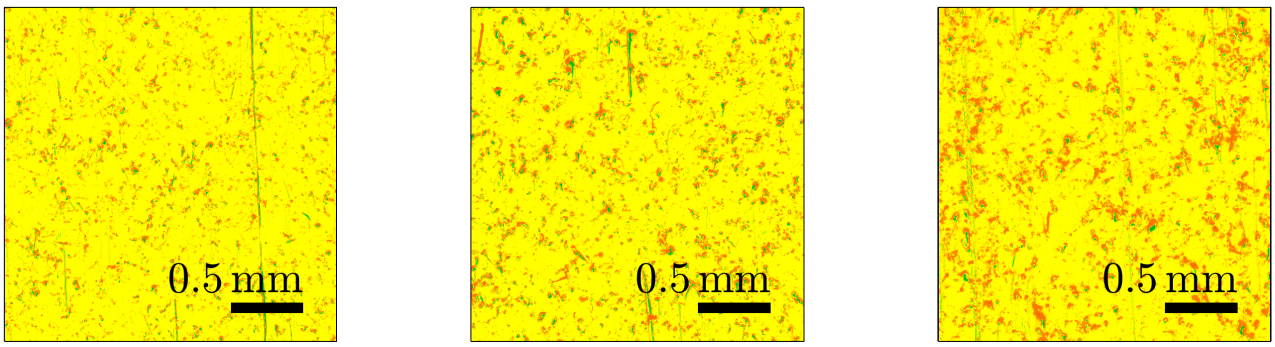

Fig. 19: Topography of the sample surface, location: middle, direction of particle movement from bottom to top, test number 0_{Cu-DHP} (left), 0 (center) and 0_{dry} (right)

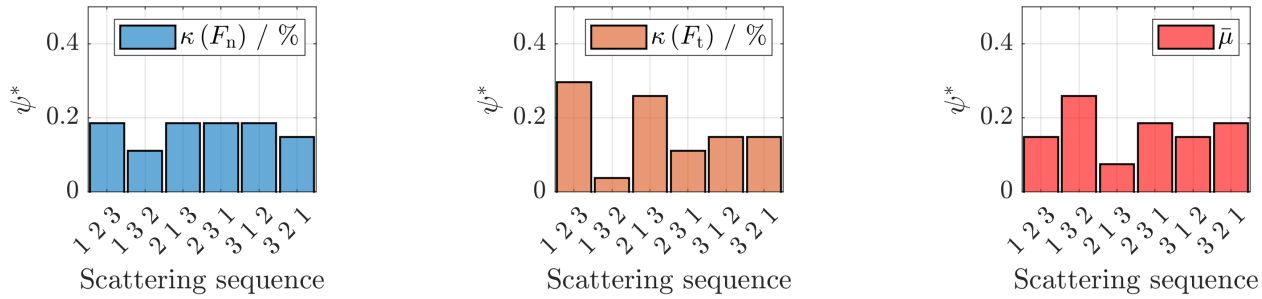

Fig. 20: Relative frequency of occurrence ψ^* of the scattering sequence of the result variables $\kappa\,(F_\mathrm{n})$ (left), $\kappa\,(F_\mathrm{t})$ (center) and $\bar{\mu}$ (right)

4 Conclusion

This work addresses the differences between an ideal tribometer and the realization of a tribometer. During realization, particular attention is paid to the sample holder's ability to align the sample parallel to the counter body. The design thus follows the suggestion made by Almond and Gee (1987) to eliminate one of the causes of the variability observed in tribological tests. Furthermore, experiments for the investigation of tribological systems with an intermediate medium consisting of hard silicon carbide particles and liquid are examined with respect to various factors, in particular the particle size, the particle area coverage ratio, the external load and the sliding speed. In particular, the relative spread of the forces exhibits a high repeatability and shows more significant effects as a result of factor changes than can be observed with the coefficient of friction, for example. In this respect, the relative spread can be used as a simple, supplementary criterion to check the comparability of the test conditions of two data sets or to detect differences between two data sets. The coefficient of friction also shows tendencies, but exhibits comparatively greater scatter. The interpretations of the observations are consistent with the surface topographies recorded and the results of the center point variants (other counter body material or without liquid). The topographies of the sample surfaces indicate that the particles predominantly roll instead of slide in almost all tests.

The investigation of the influence of the execution sequence used here is a reasonable alternative to the established procedure with random execution sequence in order to minimize the potential for error due to the carryover of particles in measurement series with different particle sizes.

Other measures, e. g. based on the frequency spectrum of the occurring forces, could also be used to check force measurement data from different tests for similarity. However, such a measure must be properly defined so that it has a high repeatability and factor dependence in order to be suitable for assessments.

References

E.A. Almond and M.G. Gee. Results from a u.k. interlaboratory project on dry sliding wear. *Wear*, 120(1):101–116, November 1987. ISSN 0043-1648. doi: 10.1016/0043-1648(87)90136-0.

Klaus Backhaus, Bernd Erichson, Sonja Gensler, Rolf Weiber, and Thomas Weiber. *Multivariate Analysemethoden: Eine anwendungsorientierte Einführung*. Springer Fachmedien Wiesbaden, 2023. ISBN 9783658404659. doi: 10.1007/978-3-658-40465-9.

Herbert Bernstein. *Messelektronik und Sensoren: Grundlagen der Messtechnik, Sensoren, analoge und digitale Signalverarbeitung*. Springer Fachmedien Wiesbaden, 2024. ISBN 9783658389291. doi: 10.1007/978-3-658-38929-1.

Raphael Bilz and Kristin M. de Payrebrune. Investigation of the influence of velocity in a tribological three-body system containing a single layer of rolling hard particles from a mechanical point of view. *Tribology International*, page 106948, 2021. doi: 10.1016/j.triboint.2021.106948.

Peter J Blau. The significance and use of the friction coefficient. *Tribology International*, 34(9):585–591, September 2001. ISSN 0301-679X. doi: 10.1016/s0301-679x(01)00050-0.

Y. P. Chang, M. Hashimura, and D. A. Dornfeld. An investigation of material removal mechanisms in lapping with grain size transition. *Journal of Manufacturing Science and Engineering*, 122(3):413–419, jan 2000. doi: 10.1115/1.1286471.

Horst Czichos and Karl-Heinz Habig, editors. *Tribologie-Handbuch*. Springer Fachmedien Wiesbaden, 2020. doi: 10.1007/978-3-658-29484-7.

R.S. Dwyer-Joyce, R.S. Sayles, and E. Ioannides. An investigation into the mechanisms of closed three-body abrasive wear. *Wear*, 175(1–2):133–142, June 1994. ISSN 0043-1648. doi: 10.1016/0043-1648(94)90176-7.

Ekbert Hering and Gert Schönfelder, editors. *Sensoren in Wissenschaft und Technik: Funktionsweise und Einsatzgebiete*. Springer Fachmedien Wiesbaden, 2023. ISBN 9783658394912. doi: 10.1007/978-3-658-39491-2.

Kenneth Holmberg and Ali Erdemir. Influence of tribology on global energy consumption, costs and emissions. *Friction*, 5(3): 263–284, sep 2017. doi: 10.1007/s40544-017-0183-5.

Fritz Klocke. *Fertigungsverfahren 2*. Springer-Verlag GmbH, 2017. ISBN 9783662533109. URL https://www.ebook.de/de/product/33169456/fritz_klocke_fertigungsverfahren_2.html.

Yulong Li, Paul Schreiber, Johannes Schneider, and Christian Greiner. Tribological mechanisms of slurry abrasive wear. *Friction*, 11(6):1079–1093, July 2022. ISSN 2223-7704. doi: 10.1007/s40544-022-0654-1.

Josef Prost, Guido Boidi, Thomas Lebersorger, Markus Varga, and Georg Vorlaufer. Comprehensive review of tribometer dynamics-cycle-based data analysis and visualization. *Friction*, 10(5):772–786, September 2021. ISSN 2223-7704. doi: 10.1007/s40544-021-0534-0.

Bikram Jyoti Sahariah, Nitesh Vashishtha, and S G Sapate. Effect of abrasive particle size on friction and wear behaviour of HVOF sprayed WC-10co-4cr coating. *Materials Research Express*, 5(6):066424, jun 2018. doi: 10.1088/2053-1591/aacd39.

Karl Siebertz, David van Bebber, and Thomas Hochkirchen. *Statistische Versuchsplanung*. Springer Berlin Heidelberg, 2017. ISBN 9783662557433. doi: 10.1007/978-3-662-55743-3.

G. W. Stachowiak. *Engineering Tribology*. Elsevier, Oxford, 2014. ISBN 9780123970473. doi: 10.1016/c2011-0-07515-4.

G.B Stachowiak and G.W Stachowiak. The effects of particle characteristics on three-body abrasive wear. *Wear*, 249(3-4):201–207, may 2001. doi: 10.1016/s0043-1648(01)00557-9.

Nitesh Vashishtha and S. G. Sapate. Abrasive wear maps for high velocity oxy fuel (HVOF) sprayed WC-12co and cr 3 c 2 -25nicr coatings. *Tribology International*, 114:290–305, oct 2017. doi: 10.1016/j.triboint.2017.04.037.

J A Williams and A M Hyncica. Abrasive wear in lubricated contacts. *Journal of Physics D: Applied Physics*, 25(1A):A81–A90, January 1992a. ISSN 1361-6463. doi: 10.1088/0022-3727/25/1a/015.

J.A. Williams and A.M. Hyncica. Mechanisms of abrasive wear in lubricated contacts. *Wear*, 152(1):57–74, January 1992b. ISSN 0043-1648. doi: 10.1016/0043-1648(92)90204-l.

F. Yates. Contingency tables involving small numbers and the χ^2 test. *Supplement to the Journal of the Royal Statistical Society*, 1 (2):217, 1934. ISSN 1466-6162. doi: 10.2307/2983604.

B. F. Yousif, Umar Nirmal, and K. J. Wong. Three-body abrasion on wear and frictional performance of treated betelnut fibre reinforced epoxy (t-BFRE) composite. *Materials & Design*, 31(9):4514–4521, oct 2010. doi: 10.1016/j.matdes.2010.04.008.